PNAS
www.pnas.org

Supplementary Information for

How the Phage T4 Injection Machinery Works including Energetics, Forces, and Dynamic Pathway

Ameneh Maghsoodi, Anupam Chatterjee, Ioan Andricioaei, Noel C. Perkins

Corresponding author: Noel C. Perkins
Email: ncp@umich.edu

This PDF file includes:

Methods
Figures S1 to S7
Table S1
Legend for Movie S1
SI References

Other supplementary materials for this manuscript include the following:

Movie S1

www.pnas.org/cgi/doi/10.1073/pnas.1909298116

Supplemental Methods

The system-level model for T4 interacting with a host cell is constructed from component models for the virus and the host. The component models include those describing the contractile (elastic) sheath and the (rigid) neck/capsid/tail tube assembly of the virus interacting with a (viscoelastic) host cell. Embedded within the system model are four energy dissipation mechanisms. These component models are summarized below and are further organized into the mechanisms that power and dissipate energy.

Dynamic Modeling of the Phage T4 Injection Machinery

During injection, the sheath undergoes a large, nonlinear conformational change from a high-energy extended conformation to a low-energy contracted conformation. It is the sudden release of the internal energy stored in the extended sheath that powers the injection machinery. This energetic release and the associated conformational change are captured in the following continuum model approximation of the contractile sheath structure.

Continuum Model of the Sheath Strands

The continuum model recognizes that the sheath as composed of six interacting helical protein strands, each of which is modeled as an elastic (Kirchhoff) rod coupled to its nearest neighbors. The resulting shell-like structure for the sheath is coupled to a rigid and massive body representing the capsid/DNA/neck/tube assembly at the upper end and to a baseplate at the lower end. The governing dynamical equations of the ith helical strand (rod) are [1]

$$\left\{\frac{\partial \boldsymbol{f}}{\partial s} + \boldsymbol{\kappa} \times \boldsymbol{f} = m_s \left(\frac{\partial \boldsymbol{v}}{\partial t} + \boldsymbol{\omega} \times \boldsymbol{v}\right) - \boldsymbol{F}_{body}\right\}^i, \tag{1}$$

$$\left\{\frac{\partial \boldsymbol{q}}{\partial s} + \boldsymbol{\kappa} \times \boldsymbol{q} = \boldsymbol{I}_s \frac{\partial \boldsymbol{\omega}}{\partial t} + \boldsymbol{\omega} \times \boldsymbol{I}_s \boldsymbol{\omega} + \boldsymbol{f} \times \boldsymbol{a}_3 - \boldsymbol{Q}_{body}\right\}^i, \tag{2}$$

$$\left\{\frac{\partial \boldsymbol{v}}{\partial s} + \boldsymbol{\kappa} \times \boldsymbol{v} = \boldsymbol{\omega} \times \boldsymbol{a}_3\right\}^i, \tag{3}$$

$$\left\{\frac{\partial \boldsymbol{\omega}}{\partial s} + \boldsymbol{\kappa} \times \boldsymbol{\omega} = \frac{\partial \boldsymbol{\kappa}}{\partial t}\right\}^i, \qquad i = 1, 2, \ldots, 6. \tag{4}$$

Equations (1) and (2) describe the balance laws for linear and angular momentum, respectively, and Eqs. (3) and (4) describe constraints on rod inextensibility and rotation, respectively. Therein, $\boldsymbol{\omega}^{\boldsymbol{i}}(s,t)$ is the angular velocity of the strand cross section, $\boldsymbol{v}^{\boldsymbol{i}}(s,t)$ is the translational velocity of the strand cross section centroid, and $\boldsymbol{\kappa}^{\boldsymbol{i}}(s,t)$ is the strand curvature/twist vector. The quantities $\boldsymbol{f}^{\boldsymbol{i}}(s,t)$ and $\boldsymbol{q}^{\boldsymbol{i}}(s,t)$ denote the strand internal force and internal moment, respectively, $m_s^i(s)$ is the strand mass per length, and $\boldsymbol{I}_s^i(\mathrm{s})$ denotes the (diagonal 3×3 tensor) strand principal mass

moments of inertia per length. Finally, $\boldsymbol{a_3^i}$ is the unit tangent vector at each cross section, and $\boldsymbol{F}^i_{body}(s,t)$ and $\boldsymbol{Q}^i_{body}(s,t)$ denote the sum of all distributed external body forces per length and moments per length, respectively. In Eq. (2), the internal moment $\boldsymbol{q^i}(s,t)$ is proportional to the curvature/twist vector through a linear elastic constitutive law

$$\boldsymbol{q^i}(s,t) = \boldsymbol{B^i}(\boldsymbol{\kappa^i} - \boldsymbol{\kappa_0}^{\boldsymbol{i}}) \,, \tag{5}$$

where $\boldsymbol{\kappa_0}^{\boldsymbol{i}}$ is the known intrinsic curvature/twist vector of the ith helical strand in the stress-free state of the sheath which is assumed to be the contracted conformation. Here, $\boldsymbol{B^i}(s,t)$ is a diagonal 3×3 stiffness tensor

$$\boldsymbol{B^i} = \begin{bmatrix} B^i & 0 & 0 \\ 0 & B^i & 0 \\ 0 & 0 & T^i \end{bmatrix}. \tag{6}$$

for the ith strand composed of the bending stiffness, B, and torsional stiffness, T, constants. These elastic stiffness constants are estimated from the molecular dynamic (MD) simulations as described next.

Estimating the Elastic Properties of the Sheath Strands

The equivalent bending/torsional elastic stiffness of the sheath strands (rods), denoted B and T above, are estimated from MD simulated thermal fluctuations of a fraction of the sheath in both the extended and contracted conformations using CHARMM. In the MD simulations, the crystal structure (3.5 Å resolution) of a single ring hexamer in both the extended and contracted conformations are obtained from the protein data bank (PDB ids 3FOH and 3FOI [2], respectively). The ring monomer gp18 in the available structures is missing the vital inner C-terminal domain, which is necessary to preserve the sheath geometry during MD simulations. The program MODELLER [3] is employed to generate a homology model of the missing residues based on the known structure of the R2-pyocin monomer [4]. The structure of the full gp18 monomer is then reconstructed by superposing the atomic structure of the homology models on a superposition of the R2-pyocin and partial gp18 monomers using the CLICK algorithm [5]. Finally, the resultant full gp18 model is oriented in the same orientation as the original hexamer, and then the hexamer is fitted into the cryo-EM maps of the extended and contracted sheath [6] using the program UCSF Chimera [7]. A fraction of the full sheath consisting of four rings is created from the single ring using published sheath helical parameters [6]; see Fig. S1. The four-ring sheaths are then used as input for Langevin dynamics applied on the non-hydrogen atoms with a friction coefficient of 5 ps^{-1}. NAMD package [8] using the CHARMM 36 all-atom force field [9] is used to generate the dynamical trajectories. A generalized Born solvent model is employed to implicitly represent the solvent. After minimization, the system is heated to a temperature of

298 K, followed by an unconstrained equilibration run of 15 ns. A 15 ns production run is used to generate the trajectories used in the calculations below.

The twist and curvature of the subunits is equal to the geometrical torsion and curvature of the (instantaneous) helix passing through the mass centers of the subunits (Fig. S1). To compute the twist and curvature of the subunits, a best-fit (least-squares) helix is constructed at each integration time step for each helical strand fragment to deduce its geometric torsion and curvature. The curvature κ_c, and geometric torsion κ_t, are computed during the 15 ns production run for each of the six strand fragments. The bending stiffness B, and the torsional stiffness T, for each strand are computed from the equilibrium fluctuations from the trajectories following the equipartition theorem of classical statistical mechanics [1]

$$\left(\frac{B}{k_B \mathcal{T}}\right)^{-1} = \langle (\kappa_c - \langle \kappa_c \rangle)^{tr} \, (\kappa_c - \langle \kappa_c \rangle) \rangle_{thermal} \tag{7}$$

$$\left(\frac{T}{k_B \mathcal{T}}\right)^{-1} = \langle (\kappa_t - \langle \kappa_t \rangle)^{tr} \, (\kappa_t - \langle \kappa_t \rangle) \rangle_{thermal} \tag{8}$$

where $\mathcal{T}$ is the ambient temperature (298 K), k_B is the Boltzmann constant, $\langle \quad \rangle$ denotes averaging over time, and $(\,)^{tr}$ stands for transpose. The MD-derived stiffness constants are reported in Table S1. Importantly, these constants describe the stiffness originating from both inter- and intra-strand interactions. For more details on the MD simulations, refer to [1].

The Initial and Boundary Conditions of the Sheath Strands

In the dynamic model of the phage T4 injection machinery, the sheath is modeled as six interacting sheath strands (elastic rods) and the remainder of the injection machinery is incorporated through the boundary conditions for the sheath strands. In particular, the sheath strands (rods) connect to the baseplate at the lower end and then to a (massive) rigid body representing the capsid/DNA/neck/tube assembly at the upper end. Accordingly, the boundary conditions at the lower end ($s = 0$) are given by [1]

$$v_{e1}^i(0,t) = v_{r0}(t)\,, \qquad v_{e2}^i(0,t) = 0\,, \qquad v_{e3}^i(0,t) = 0, \tag{9}$$

$$q_{e1}^i(0,t) = 0, \qquad \omega_{e2}^i(0,t) = 0, \qquad \omega_{e3}^i(0,t) = 0\,, \quad i = 1,2,..,6. \tag{10}$$

Equation (9) describes the fact that, at the baseplate, the strands remain stationary except along the radial direction where the sheath expands radially during contraction. Equation (10) describes that the strands cannot rotate at the baseplate except about the radial direction. The boundary conditions at the upper end ($s = L(t)$) are given by [1]

$$v_{e1}^{i}(L,t) = v_{rl}(t)\ , \quad v_{e2}^{i}(L,t) = r_{e1}^{i}(L,t)\,\omega_{e3}^{i}(L,t)\ , \tag{11}$$

$$\omega_{e2}^{i}(L,t) = 0\ , \quad q_{e1}^{i}(L,t) = 0\ , \tag{12}$$

$$\sum_{i=1}^{6} f_{e3}^{i}(L,t) + F_{drag}(t) + F_{cell}(t) + F_{tube}(t) = m_c \frac{\partial v_c(t)}{\partial t}, \tag{13a}$$

$$\sum_{i=1}^{6} q_{e3}^{i}(L,t) + \sum_{i=1}^{6} \left[\boldsymbol{r}^{i}(L,t) \times \boldsymbol{f}^{i}(L,t)\right]_{e3} + Q_{drag}(t) + Q_{cell}(t) + Q_{tube}(t) = I_c \frac{\partial \omega_c(t)}{\partial t}. \tag{13b}$$

Equation (11) describes the fact that, at the upper end, the sheath expands radially and rotates about the tail tube axis during contraction and (12) describes that the angular rate about the circumferential direction vanishes whereas the strand cross section is free to rotate about the radial direction. Equation (13a,b) represent the balance laws of linear (13a) and angular (13b) momentum governing the rigid body motion of the attached capsid/neck/tail tube assembly which possesses two degrees of freedom. In particular, this assembly translates along the tail tube axis with velocity $v_c(t) = v_{e3}^{i}(L(t),t)$ and rotates about this axis with angular velocity $\omega_c(t) = \omega_{e3}^{i}(L(t),t)$. The quantities F_{drag} and Q_{drag} are the external hydrodynamic drag force and moment from the surrounding environment on the capsid, F_{cell} and Q_{cell} are the reaction force and moment from the cell membrane on the tip of the tail tube, and F_{tube} and Q_{tube} are the frictional force and moment between sheath and tail tube which are incorporated in the upper boundary condition (13) as described in detail below.

Note that the sheath starts its extended (pre-stressed) conformation and that this conformation serves as the initial condition for the subsequent simulation of the injection process. Numerical solutions of the governing dynamical Eqs. (1-5) and incorporating the initial and boundary conditions are obtained using space-time finite differencing following the methodology outlined in [1]. Doing so yields the four-vector unknowns $\{\boldsymbol{v}^{i}, \boldsymbol{\omega}^{i}, \boldsymbol{\kappa}^{i}, \boldsymbol{f}^{i}\}$ for each of the six interacting strands.

Internal Energy that Powers the Injection Machinery

Before contraction, the sheath is locked in the high-energy extended conformation. The energy required for the tip of the tail tube to pierce the host cell derives from the sudden release of the energy (entropy and enthalpy) stored in the extended sheath during contraction.

In our model, the enthalpy of the sheath is represented by the strain (elastic) energy of the six interacting strands. The enthalpy of the sheath (in any state during contraction) is given by the strain energy of the six interacting helical protein strands per

$$U(t) = \sum_{i=1}^{6} \int_{0}^{L} \frac{1}{2} \left(\boldsymbol{\kappa^i} - \boldsymbol{\kappa_0}^{\boldsymbol{i}}\right)^{tr} \boldsymbol{B^i} \left(\boldsymbol{\kappa^i} - \boldsymbol{\kappa_0}^{\boldsymbol{i}}\right) \mathrm{d}s. \tag{14}$$

The entropic contribution of sheath contraction can be estimated by computing the difference in entropy for the sheath in the extended versus the contracted state using the covariance matrices of the atomic fluctuations as given by [10]

$$\mathcal{T}(S_{ext} - S_{cont}) = \mathcal{T} k_B \sum_{i=1}^{m} \left\{ \frac{\hbar\omega_i / k_B \mathcal{T}}{e^{\hbar\omega_i / k_B \mathcal{T}} - 1} - \ln\left(1 - e^{-\hbar\omega_i / k_B \mathcal{T}}\right) \right\} \tag{15}$$

Where $\hbar$ is Planck's constant and ω_i denotes the natural (vibrational) frequencies of sheath structure in the extended and contracted states which can be estimated from a coarse-grained model of the sheath. That model considers that the six strands (composed of the gp18 subunits) form a hollow cylindrical sheath having the bending and torsional stiffness coefficients reported in Table S1. Accordingly, we approximate the sheath structures as a hollow elastic rod that is clamped at both ends, recognizing its attachment to the massive (hence largely immobile) capsid at one end and the similarly immobile host cell at the opposite end. For this model, the natural frequencies for the bending (ω_{ib}) and torsional (ω_{it}) modes of the sheath are given by [11]

$$\omega_{ib} = x_i^2 \sqrt{\frac{B}{\rho A_r {L_r}^4}}, \qquad x_i = (2i+1)\pi/2. \tag{16}$$

$$\omega_{it} = \frac{i\pi}{L_r} \sqrt{\frac{T}{\rho J_r}}, \qquad i = 1, 2, 3, \ldots.$$

where A_r being the cross-sectional area, J_r the cross-sectional polar moment of area, L_r the length, and ρ the mass density of the sheath structure. Substituting the natural frequencies from Eq. (16) into Eq. (15) yields an estimate of entropic contribution of sheath contraction.

Note that Eq. (15) represents the summation over the natural frequencies. To determine the requisite number of modes m for inclusion in Eq. (15), we consider the difference in the wavelengths of the modes for the extended and contracted confirmations [12]. At the higher order modes, the associated wavelengths of the extended sheath become indistinguishable from those of the contracted sheath. Consequently, it is the lower order modes that control the entropic contribution. When the differences become less than 1% of the initial difference, then the further contribution from higher order modes are minor [12]. Doing so reveals that one should include the first 70 modes (including both bending and torsional modes) of the extended and contracted states. With 70 modes included, the estimated enthalpic contribution is 200 kT which is negligibly small relative to enthalpic of 14,500 kT contribution estimated from Eq. (14). We describe next how the internal energy is released through a contraction wave that propagates through the sheath from the baseplate to the neck.

Non-Homogeneous Sheath Stiffness and Dynamic Contraction Wave

Moody [13] hypothesized that the sheath first contracts where it attaches to the baseplate and then sequentially through the sheath towards the neck through a (displacive) contraction wave, a hypothesis consistent with experimental images of intermediate states of T4 captured during contraction events. In this mechanism, the sheath-tail tube interactions are broken sequentially from the baseplate towards the neck allowing the sheath subunits to form new intra- and inter-strand contacts. These new contacts are responsible for the marked differences in the strand elastic stiffness constants between the fully extended and fully contracted conformations as reported in Table S1. Consistent with this mechanism, for a *partially* contracted sheath (see Fig. 7A(II)), one would expect a non-homogeneous sheath stiffness $\boldsymbol{B}$ with the region closest to the baseplate possessing stiffness parameters close to those of the contracted conformation and the region closest to the neck possessing stiffness parameters close to those of the extended conformation. We capture the expected non-homogeneous stiffness property of the sheath, introduced as the stiffness tensor $\boldsymbol{B}$ in Eq. (6) in the model, as follows.

The contraction process is initiated in the model by prescribing the radial velocity v_{r0} appearing in the boundary condition (9) to rapidly expand the baseplate. As a result, the capsid/neck/tail tube assembly begins to translate towards the baseplate. We denote this translation by the parameter $0 \leq h_c \leq H$, which measures the state of contraction between the limits of the fully extended conformation ($h_c = 0$) and the fully contracted conformation ($h_c = H \cong 500$ Å). The non-homogenous stiffness tensor of the strands forming the sheath is modeled per

$$\boldsymbol{B}(s, h_c) = \boldsymbol{B_e} + (\boldsymbol{B_c} - \boldsymbol{B_e})\left(1 - e^{\frac{-\alpha h_c}{H - h_c}}\right), \quad \alpha(s) = \frac{(\alpha_L - \alpha_0)s}{L} + \alpha_0 \tag{17}$$

where $\boldsymbol{B_e}$ and $\boldsymbol{B_c}$ denote the limiting stiffness tensors for the extended and contracted sheaths, respectively, and as composed by the values reported in Table S1. The linear function $\alpha(s)$ controls an exponential increase in the stiffness tensor from that of the extended state to that of the contracted state as determined by the two rate parameters (α_0, α_L). The rate parameter α_L controls the (initially slower) increase in stiffness at the neck ($s = L$) whereas the rate parameter α_0 controls the (initially rapid) increase in stiffness at the baseplate ($s = 0$). In this study, we select $\alpha_0 = 5$ and $\alpha_L = 1$. Figure S2 illustrates the variation of bending and torsional stiffness coefficients along the sheath strands as a function of contraction h_c.

Note that the Eq. (17) is chosen to be consistent with Moody's micrographs in Fig. 7A and the MD-derived elastic stiffness in Table S1. From Fig. 7A(I), the fully extended sheath is a largely uniform structure, and so the elastic stiffness of the strands is homogenous and equal to the extended stiffness values in Table S1; see B_{ext} and T_{ext} in Fig. S2 when $h_c = 0$. Similarly, from Fig. 7A(III), the fully contracted sheath is also a largely uniform structure, and so the elastic stiffness of the strands is again homogenous and equal to the contracted stiffness values in Table S1; see B_{cont} and T_{cont} in Fig. S2 when h_c= 500 Å. During contraction, the intermediate sheath is partially contracted and partially extended as illustrated in Fig. 7A(II), and so the elastic stiffness is non-homogeneous along the sheath strands. More specifically, the contracted region close to the baseplate is stiffer than the extended region close to the neck. For example, at the intermediate

contraction length h_c= 200 Å in Fig. S2 the bending/torsional stiffness for the lowest subunit ($s = 0$ at the baseplate) is greater than that for the uppermost subunit ($s = L$ at the neck). This non-homogeneous stiffness distribution is modeled using Eq. (17). Note, any other function that satisfies these requirements would yield similar results. Moreover, the dynamics of the simulated injection process is actually quite insensitive to the choice of the rate parameters (e.g., the ratio α_0/α_L influences the injection time only on the microsecond time scale).

During sheath contraction, the arc length L of the sheath strands increases by approximately 400 Å and this increase is also captured in the model. We employ an interpolation function for L that is analogous to that used in Eq. (17) for the stiffness tensor, as both the stiffness and length of the strands are controlled by the same (displacive) process. In particular,

$$L(h_c) = L_e + (L_c - L_e)\left(1 - e^{\frac{-\beta h_c}{H - h_c}}\right), \tag{18}$$

where L_e and L_c denote the limiting strand arc lengths for the extended and contracted conformations, respectively. The parameter β controls the exponential increase in the strand arc length and the value $\beta = 0.2$ was selected for the simulations reported herein. Again, the time scale of the injection dynamics is largely insensitive to this choice.

Below, we extend the dynamic modeling approach to yield a system-level model of T4 interacting with a host cell. In particular, we couple the above model for T4 to a viscoelastic model of the host cell through the reaction force of the host on the tip of the tail tube. Doing so enables one to estimate the force that T4 exerts on the host and, ultimately, the conditions that lead to rupture of the outer cell membrane during the injection process.

Mechanisms that Dissipate Energy During Injection

The system model of T4 interacting with a host cell accounts for four likely mechanisms that dissipate energy during the injection process. These mechanisms include: 1) the hydrodynamic dissipation on the capsid and sheath from the surrounding environment, 2) the internal (material) dissipation of the sheath strands during the large conformational change, 3) the dissipation from the host cell membrane interacting with the tip of the tail tube, and 4) the hydrodynamic interactions between the flexible sheath and the tail tube during contraction. We summarize the models for each mechanism in turn.

Hydrodynamic Dissipation on Capsid and Sheath

During contraction, the capsid and the sheath are subject to nanoscale hydrodynamic drag forces and moments from the surrounding fluid environment which are modeled using classical Stoke's regime drag (Reynolds number << 1). Accordingly, the hydrodynamic drag force and moment from the surrounding fluid environment on the capsid are given by [14]

$$F_{drag} = -C_t v_c \,, \quad C_t = \frac{2\,\pi\,\eta\,l}{\ln\left(\frac{l}{2R_c}\right)-0.2} \tag{19}$$

$$Q_{drag} = -C_r \omega_c \,, \quad C_t = 4\eta\pi l {R_c}^2$$

where, ω_c is the angular velocity and v_c is the linear velocity of the capsid, and l is the length and R_c is the radius of the capsid. The parameters C_t and C_r are the force and moment drag coefficients, respectively, and η denotes the viscosity of bulk water. This drag force/moment pair on the capsid is incorporated in the upper boundary conditions of sheath strands as noted in (13).

Similarly, the hydrodynamic drag force/moment per unit length on the ith strand of the sheath from the surrounding fluid environment are given by

$$\boldsymbol{F}^i_{body} = -\begin{bmatrix} c_{t1} & 0 & 0 \\ 0 & c_{t2} & 0 \\ 0 & 0 & c_{t3} \end{bmatrix} v^i, \qquad \boldsymbol{Q}^i_{body} = -\begin{bmatrix} 0 & 0 & 0 \\ 0 & 0 & 0 \\ 0 & 0 & c_{r3} \end{bmatrix} \omega^i \tag{20}$$

where the drag coefficients are [14]

$$c_{t1} = \frac{4\pi\eta}{ln\left(\frac{L}{2R_s}\right) + 0.84}, \qquad c_{t2} = c_{t1}, \quad c_{t3} = \frac{2\pi\eta}{ln\left(\frac{L}{2R_s}\right) - 0.2}, \tag{21}$$

$$c_{r3} = 4\pi\eta {R_s}^2$$

Here, R_s=R_s(t) and $L = L(t)$ denote the radius and contour length of each strand (rod), respectively, and η is again the viscosity of bulk water. The drag force/moment pair on the sheath strands is incorporated in the balance laws for linear (1) and angular (2) momentum through the terms $\boldsymbol{F}^i_{body}$ and $\boldsymbol{Q}^i_{body}$ defined by (20).

Internal Dissipation of Sheath Strands

During sheath contraction, the component helical protein strands undergo a nonlinear conformational change from the extended conformation to the contracted conformation. The associated large deformations of the sheath strands induce internal friction through the rearrangement of the sheath (gp 18) protein subunits. One could model this internal friction by replacing the prior linear elastic constitutive law for the sheath strands (5) with a viscoelastic law. With this option, the constitutive law would become a function of both curvature and twist as well

as the time rate of change of curvature and twist, which increases the computational cost considerably. As an alternative, another option is to approximate the internal dissipation of sheath as an equivalent hydrodynamic drag from the surrounding fluid defined by a new drag coefficient η_{int} and at little computational cost. To this simpler end, we summarize below how to estimate the equivalent drag coefficient η_{int} required in the Stoke's drag model (Note, Reynolds number << 1). We refer interested readers to our previous work [15] which details how to calculate the internal viscosity coefficients for biofilaments.

Energy dissipation for a biofilament (such as the helical protein strands of the sheath) can be quantified by studying the autocorrelation of the transverse displacement u of the biofilament during thermal fluctuations assuming ideal (white) thermal noise. If we assume an equivalent external dissipation representing the internal dissipation of biofilament, then the associated autocorrelation $\mathcal{R}(t)$ for u and its relaxation time τ is given by [15]

$$\mathcal{R}(t) = \mathrm{R}\exp\left(\frac{-t}{\tau}\right) \tag{22}$$

$$\tau = \eta_{int}\frac{(\kappa S + Bq^2)}{\kappa S B q^4} \tag{23}$$

where η_{int} is the dissipation coefficient of equivalent external drag, t is the lag-time, κ denotes the shear correction factor $S = GA$ for Timoshenko beam theory which is the product of the filament shear modulus G and cross sectional area A, and where $B = EI$ is the filament bending stiffness which is the product of the filament Young's modulus E and area moment of inertia I.

Note that the thermal fluctuations in one ring of the tail sheath (having relatively large radius compared to the amplitude of the thermal fluctuations) mimic transverse thermal fluctuations of a (nominally straight) filament [16]. The radial displacement of the ring is analogous to the transverse displacement of the filament. Accordingly, for thermal fluctuations of one ring of the sheath, the autocorrelation of the radial displacement $u(t)$ and its relaxation time are given by Eqs. (22-23). We utilize these results to analyze the thermal fluctuations of a ring of the tail sheath obtained from atomistic (MD) simulations. We employ a similar MD procedure described above to simulate a four-ring portion of the sheath, and then calculate the transverse fluctuations $u(t)$ for one of the middle rings as a representative (circular) filament for the T4 sheath structure; refer to Fig. S3. A middle ring is chosen to minimize solvent surface effects on the radial fluctuations. Transverse fluctuations $u(t)$ are defined as the radial fluctuations from the best-fit circle passing through the center of masses of the six subunits of the ring; refer to Fig. S3. For each frame of the trajectory, the center and radius $\langle r(t)\rangle$ of the best-fit circle was calculated with the radial deflection $u(t)$ being the deviation $u(t) = r(t) - \langle r(t)\rangle$. The autocorrelation function $\mathcal{R}(t) = \langle u(t), u(t + t)\rangle$ is then calculated from the trajectories for both the extended and the contracted conformations. Fitting a one-exponential function (22) for $\mathcal{R}(t)$ for the extended and contracted rings yields the relaxation time τ and then the equivalent dissipation coefficient η_{int} for each conformation per (23). Therefrom, the equivalent dissipation coefficient is estimated as η_{int} = 0.003 Pa.s in the extended state and η_{int} = 0.008 in the contracted state. As a further illustration of this procedure, Figure S4 shows the autocorrelation of the transverse displacement of a middle ring of the sheath

fragment in both the extended and contracted conformations using MD simulation. Superimposed on this data are the best-fit curves employing (22) from which we compute the relaxation time τ.

Finally, the (Stoke's) drag model is again employed to model the net internal dissipation as an equivalent (but now significantly increased) external hydrodynamic drag using the friction coefficient $\bar{\eta}_{int} \cong 0.005$ Pa.s which is the average across the extended and contracted conformations. These equivalent external hydrodynamic drag force and moment on sheath strands are added to (1) and (2), respectively, through the terms $\boldsymbol{F}_{body}$ and $\boldsymbol{Q}_{body}$.

Cell-Tail Tube Dissipation (and Interactions)

During sheath contraction, the tail tube simultaneously rotates and translates downward to contact and then pierce the outer membrane of the host cell. Assuming the tip of the tail tube touches the outer membrane say at time t_1, the tip then applies a reaction force and moment on the outer membrane causing it to deform locally immediately thereafter. When the tip of the tail tube finally ruptures the outer membrane say at time t_2, it then continues to translate through the periplasmic space. During this entire process, the cell applies a reaction force and moment on the tip of the tube in the forms of: 1) a coupled indentation reaction force and moment before rupturing the outer membrane (for $t_1 < t < t_2$), and 2) a coupled hydrodynamic drag force and moment from the viscous layers of the periplasmic space until the end of sheath contraction (for $t_2 < t < t_3$, where t_3 denotes the end of sheath contraction). We first introduce a viscoelastic model for cell-tube interaction before the cell rupture event (for $t_1 < t < t_2$).

Following [17], the viscoelastic behavior of the outer cell membrane is illustrated schematically in Fig. S5. This model for the outer cell membrane consists of an elastic spring with stiffness k_1 in series with a parallel spring and dashpot with stiffness k_2 and damping coefficient D_c, respectively. The governing dynamical equation for the membrane becomes

$$\frac{\mathrm{d}F_{cell}(t)}{\mathrm{d}t} + F_{cell}(t)\left(\frac{k_1 + k_2}{D_c}\right) - k_1\frac{\mathrm{d}z(t)}{\mathrm{d}t} - \left(\frac{k_1 k_2}{D_c}\right)\mathrm{z(t)} = 0, \;\; t_1 < t < t_2 \tag{24}$$

Here, $z(t)$ is the dynamic cell indentation caused by the tip of the tail tube during sheath contraction and F_{cell} is the resulting indentation force from the tube tip on the outer cell membrane. By definition, $z(t_1) = 0$ when the tip of the tail tube first contacts the outer cell membrane. Since the tail tube is (assumed) rigidly connected to the capsid (and thus also to the upper end of the sheath strands), the indentation displacement $z(t)$ and velocity $\frac{\mathrm{d}z(t)}{\mathrm{d}t}$ in (24) can be readily determined from the displacement and linear velocity of the capsid along the tube axis within the above model for the sheath and the boundary conditions at the upper end. Numerical solution of (24) yields the indentation force F_{cell} which decelerates the sheath contraction during the time interval $t_1 < \mathrm{t} < t_2$. The force F_{cell} is then added to the equation of motion of the capsid/neck/tail tube assembly to complete the coupling of these component models; refer to the upper boundary condition (13a). The dynamic viscoelastic behavior of the outer membrane of *E. coli* (strain K12)

under a constant force applied by an AFM tip reveals that $k_1 = 0.056$ N/m, $k_2 = 0.54$ N/m, and $D_c = 0.36$ N.s/m [17]. The force F_{cell} monotonically increases during indentation up to the point of rupture of the outer membrane (see Fig. 6). The rupture force for *E. coli* remains unknown. However, experimental studies [18] reveal that a pyramid tip of an AFM ruptures a lipid bilayer under forces greater than 10 nN. We hypothesize that the outer membrane of *E. coli* will rupture when the T4 tip/membrane interface achieves similar (rupture) stress to that measured for the AFM on the lipid bilayer. We then arrive at the stress at this interface by tracking the time-dependent indentation force of the tip of the tail tube on the host cell membrane, $F_{cell}(t)$, via Eq. (24) and use the known T4 tip geometry to compute the stress. Note that the maximum indentation of the outer membrane, $z(t_2)$, equals the total displacement of the tail tube at the rupture event.

While we also suspect there may be a reaction moment Q_{cell} from the outer membrane on the tail tube, we are ignoring this potential effect for lack of any present information concerning the torsional stiffness of the membrane. Accordingly, $Q_{cell} = 0$ in (13b). Should future research reveal the torsional stiffness, its influence could be readily added to (13b).

After rupturing the outer membrane, the tip of the tail tube is subject to the hydrodynamic drag from the periplasmic space for the time interval $t_2 < t < t_3$. During this latter phase, the hydrodynamic drag and moment on the tail tube is modeled by Stoke's law (Reynolds number << 1) per

$$\mathrm{F}_{cell} = -C_d(t)\, v(L,t), \quad Q_{cell} = -D_d(t)\, \omega(L,t), \qquad t = [t_2, t_3]. \tag{25}$$

Here, $v(L,t)$ and $\omega(L,t)$ are the linear velocity and angular velocity of the tube computed from the upper end of sheath strands per (11-13). Before penetration into the periplasmic space, the drag coefficients C_d and D_d are zero and they then increase with penetration depth thereafter. Thus, the instantaneously values of C_d and D_d are calculated by linear interpolation of the values at times t_2 and t_3 as given by [14]

$$C_d(t_2) = D_d(t_2) \approx 0, \tag{26}$$

$$C_d(t_3) \approx \frac{2\pi\eta_c}{ln\left(\frac{L_t}{2R_t}\right) - 0.2}, \qquad D_d(t_3) \approx 4\pi {R_t}^2\, \eta_c$$

in which η_c (~1.1 Pa.s [19]) is the viscosity of the periplasmic space, R_t is the radius of the tail tube within the periplasmic space, and L_t is the length of tail tube within the periplasmic space after full sheath contraction. The force F_{cell} and moment Q_{cell} are then added to the upper boundary conditions (13a,b).

Sheath-Tail Tube Friction

To understand the sheath-tail tube interactions, we begin by reporting the surface Coulomb potential distribution and the Kyte-Doolittle hydrophobicity [20] for the tail tube, the extended sheath, and the contracted sheath. The atomic structures of the sheath are determined following the same procedure used to study the thermal fluctuations of the sheath; refer to *Internal Dissipation of Sheath Strands*. The atomic structure of the lower two rings of the tail tube are extracted from the cryo-EM structure of the entire T4 baseplate (PDB id 5IV5), and two additional rings are constructed using the published tail tube helical parameters [21]. The surfaces are generated using UCSF Chimera [7].

As illustrated in Fig. S6A, the inner surface of the extended sheath is largely positively charged at the edges (blue) where it forms complementary charged interactions with the mostly negatively charged (red) outer tail tube surface. However, apart from these edges, the inner sheath surface is equally neutrally, positively and negatively charged. In the contracted conformation, the inner sheath edge is negatively charged, implying that during contraction there is a redistribution of charges along the inner sheath surface. Importantly, these charge distributions along the inner sheath surface for the both extended and contracted conformations and along the outer tube surface are relatively uniform. This implies that the net electrostatic and nonbonded forces remain largely perpendicular to the tube axis and thus contribute insignificant work as the tube translocates through the sheath. By contrast, significant work and interaction may arise during translocation from the viscosity of the interstitial nano-scale gap. As illustrated in Fig. S6B, the outer surface of the tail tube and the inner surface of the sheath are largely hydrophilic (blue), indicating that the nano-channel between the tube and sheath is essentially hydrophilic. Accordingly, the viscosity of this interstitial nano-scale gap is expected to be far greater than that of bulk water [22].

As illustrated in Fig. S6, the gap between the sheath and the tail tube is nearly zero in the extended state and about 10 Å in the contracted state. To simulate the friction (hydrodynamic drag) between the contracted portion of the sheath and the tube, we employ a classic model of fluid motion between two parallel surfaces with linearly varying velocity profile due to shear both parallel and perpendicular to the translating and rotating tail tube; refer to Fig. S7. Since the tail tube attaches to the upper end of the sheath strands, the tail tube rotates and translates with the same linear (v_t) and angular (ω_t) velocities of the upper end of the sheath, i.e., $v_t(t) = v(L,t)$ and $\omega_t(t)$=$\omega(L,t)$. The linear and angular velocities of the contracted portion of the sheath are almost zero. The resulting friction (viscous) forces and moments from the water molecules on the inner surface of the sheath and the outer surface of tube are given by

$$\mathrm{F}_{tube} = \eta_w \frac{v(L,t)}{d} A_t(\mathrm{t}), \tag{27a}$$

$$\mathrm{Q}_{tube} = \eta_w \frac{r_t \omega(L,t)}{d} r_t \, A_t(\mathrm{t}) \tag{27b}$$

where η_w is the effective water viscosity in the nano-scale gap d~10 Å, A_t is the wetted area of

the tube interacting with the contracted portion of the sheath, r_t is the outer radius of the tube. The frictional force F_{tube} and moment Q_{tube} in (27a) and (27b) are applied to the upper boundary condition of sheath strands given by (13a) and (13b), respectively.

Atomistic Movie of Dynamic Pathway of Injection Process

To illustrate the dynamic pathway of the injection process, we create a system-level animation of the entire T4 system employing the simulation results for the dynamic continuum model presented herein. The continuum model provides the dynamically changing shape of each of the six interacting strands of the sheath as well as the dynamic translation and rotation of the capsid/neck/tail tube assembly during the injection process. We superimpose atomistic representations of these elements using reported atomic structures of the T4 sheath, capsid, tail tube, and neck as described below.

The dynamic continuum model of the six interacting helical strands of the sheath yields the trajectories of the mass centers of the gp18 subunits as functions of time during the injection process. From these continuum-level trajectories, we select 100 equally spaced time frames over the injection time to create corresponding time frames for system-level trajectories. To start, for each of the 100 time frames, the cylindrical coordinates (i.e., radius, height and polar angle) are calculated for 23 equally-spaced points along the arc length of a single helical sheath strand using the dynamic strand conformation from the continuum model. Each point corresponds approximately to the mass center a gp18 subunit within each of the 23 hexameric rings forming the sheath.

During sheath contraction, each subunit rotates by 45 degree about its radial axis and translates outward in radial direction. The intermediate structure of each ring at each time frame is obtained in MATLAB by linear interpolations of the known ring structures for the fully extended (PDB id 3FOH) and fully contracted (PDB id 3FOI) conformations given by

$$V(j,i) = \frac{V_{cont} - V_{ext}}{r_{cont} - r_{ext}}(r(j,i) - r_{ext}) + V_{ext} \quad , \quad j = 1,2,\dots,23. \quad i = 1,2,\dots,100. \qquad (28)$$

In which V_{ext} and V_{cont} are the spatial coordinates of atoms for the extended and contracted rings, respectively, and r_{ext} and r_{cont} are the radiuses of the extended and contracted rings, respectively. Finally, r and V are the radius and spatial coordinates of atoms of the ring j at time frame i. The rings are aligned and assembled using the height and polar angle of the points along the helical strands predicted by the continuum model. The result is the full intermediate structure of the sheath for each time frame. The sheath structure is then attached to the neck, tail tube and neck to represent the structure of virus during injection process.

The atomic structure of a single ring hexamer of the tail tube is extracted from the cryo-EM structure of the entire T4 baseplate (PDB id 5IV5 [21]). The 23-ring full structure of the tail tube is then constructed in MATLAB by repeatedly applying the tail tube helical parameters (helical rise and twist 40.2 Å and 17.9 degrees [21]). A fraction of neck, gp15 hexamer, is extracted from the gp15-gp18 hexamer complex (PDB id 3J2M) [23], and the atomic structure of the full icosahedral T4 capsid is obtained from the protein data bank (PDB id 5VF3) [24]. The atomic structures of the tail tube, capsid and a section of the neck (gp15 hexamer) are attached to the sheath structure to create contraction intermediates of the entire phage (minus the baseplate, tail fibers and missing sections of the neck). Within known cryo-EM resolutions, no rearrangement of subunits of the capsid, tail tube and the neck (gp15) has been observed during contraction, and the orientation of the gp15 hexamer relative to the top of the sheath remains preserved [23]. Therefore, in the contraction intermediates, the translation and rotation of the capsid-tail tube-gp15 hexamer complex is identical to the top ring of the sheath during contraction. The resulting intermediate structures (sheath, tail tube, capsid and fraction of neck) of phage T4 at 100 time frames created by MATLAB are then imported in VMD to create the single trajectory visible in the Movie S1. Note, to enable efficient rendering of the multi-million atom trajectory, the capsid is represented by only one atom per residue in the movie. All other components of the phage are shown in all-atom representations.

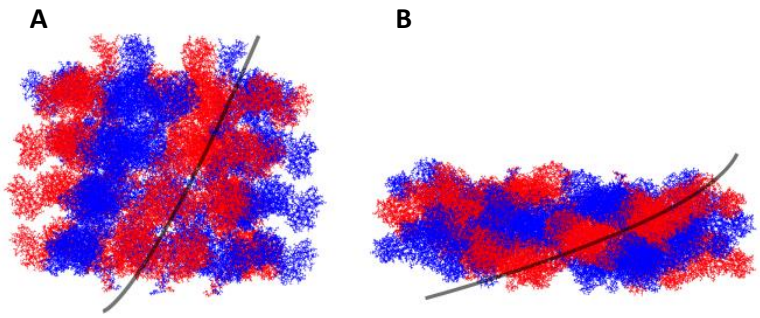

Figure S1: Four rings of gp18 subunits that form a fraction of the sheath in the extended (A) and contracted (B) conformations. The black curve denotes the best-fit helix passing through the mass centers of the subunits in one (red) strand.

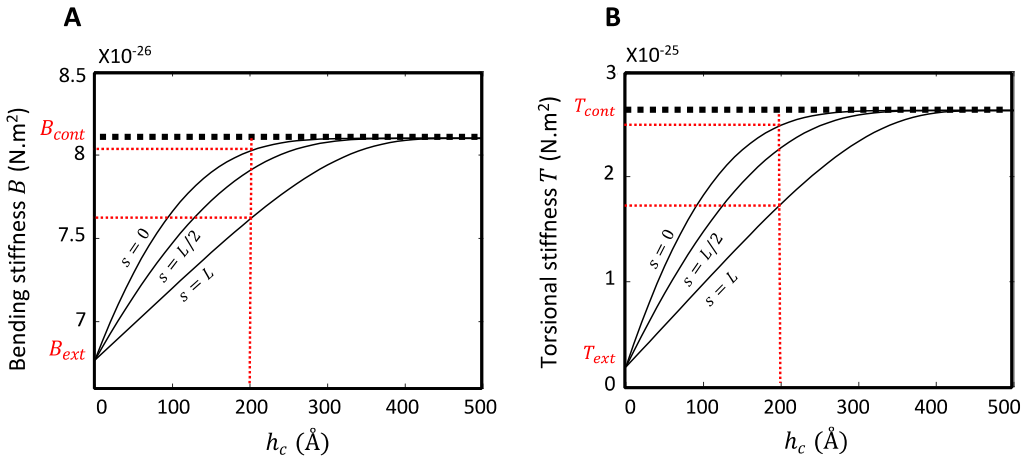

Figure S2: The non-homogenous bending (A) and torsional (B) stiffness coefficients along the sheath strands described by Eq. (17) in which $\alpha_0 = 5$ controls the rapid conformational change at the baseplate ($s = 0$) and $\alpha_L = 1$ controls the slower conformational change at the neck ($s = L$). The stiffness coefficients for all points within the sheath increase from the values for the extended sheath to those of the contracted sheath as reported in Table S1. At the intermediate contraction length, for example, $h_c = 200$ Å, the elastic stiffness for the lowest subunit ($s = 0$ connected to the baseplate) is greater than that for the uppermost subunit ($s = L$ connected to the neck).

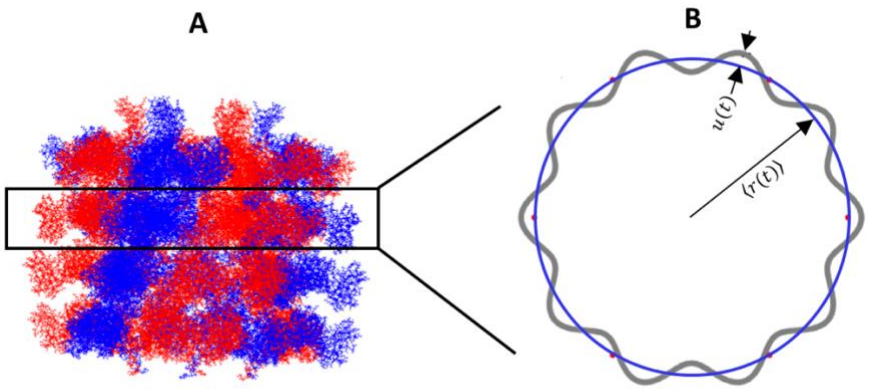

Figure S3: (A) Atomistic structure of the four-disc section of the T4 tail sheath with the middle ring surrounded by the superimposed rectangle. (B) The best-fit circle through the centers of masses (red dots) of the ring subunits of the middle ring has mean radius $\langle r(t) \rangle$. The radial fluctuations of the filament from the circle are denoted by $u(t)$.

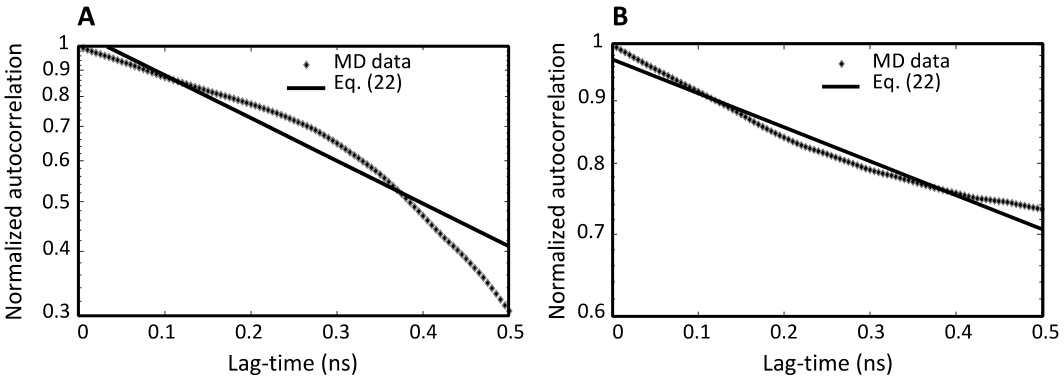

Figure S4: Autocorrelation of the transverse displacement of a middle ring of the sheath fragment from MD simulation for (A) the extended conformation and (B) the contracted conformation. The discrete data points indicate the MD-derived autocorrelation and the solid line represents the best fit per Eq. (22). Note log scale on vertical axis.

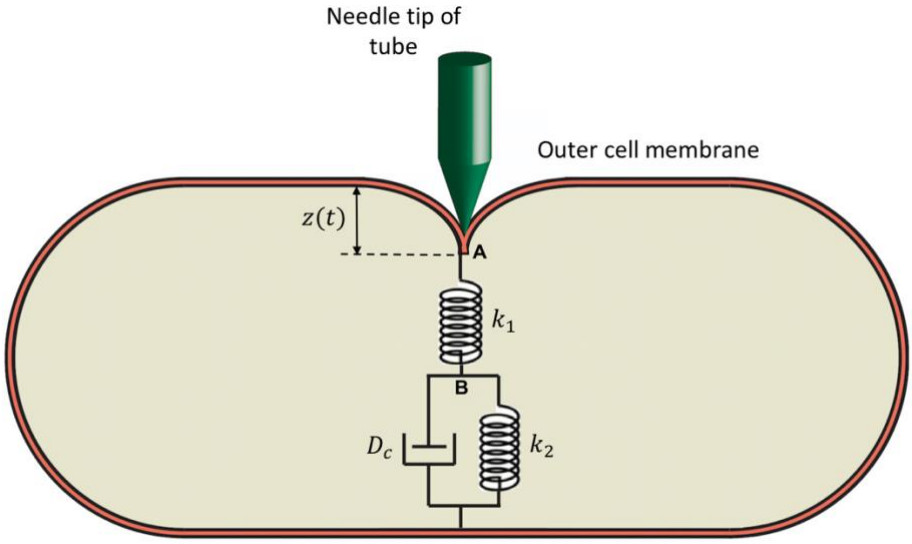

Figure S5: Schematic of tail tube-cell interaction model before rupturing the outer membrane of the cell. The viscoelastic behavior of the outer cell membrane is modeled by an elastic spring with stiffness k_1 (governing instantaneous membrane deformation) in series with a parallel spring and dashpot with stiffness k_2 and damping coefficient D_c, respectively (governing delayed membrane deformation) [17].

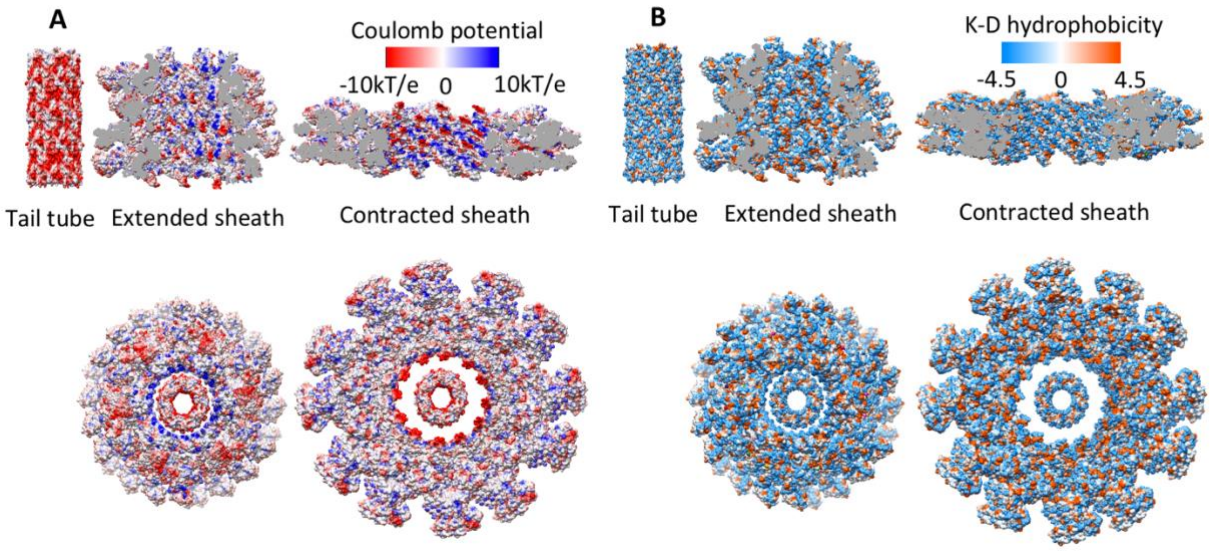

Figure S6: (A) Surface coulomb potential distribution of (clockwise) four rings of the outer surface of the tail tube, the inner surface of the extended sheath, and the inner surface of the contracted sheath. Beneath are top views of the tube within the extended sheath and within the contracted sheath. (B) Kyte-Doolittle hydrophobicity [20] of the same surfaces arranged in the same order as in (A). The outer surface of the tail tube and the inner surface of the sheath are largely hydrophilic (blue).

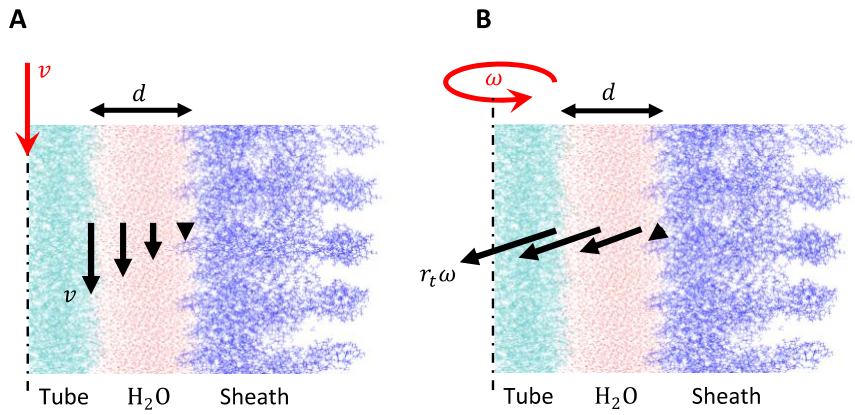

Figure S7: Components of the velocity profile of water within the nanoscale gap, d, between the sheath and the tail tube due to (A) translation v, and (B) rotation ω of the tail tube during injection.

Table S1: Elastic bending and torsional stiffness constants of the sheath strands for phage T4 in both the extended and contracted conformations from MD simulations.

Conformation	Bending stiffness ($10^{-27}\mathrm{N.m^2}$)	Torsional stiffness ($10^{-27}\mathrm{N.m^2}$)
Extended sheath, gp18 strand	67.7	18.9
Contracted sheath, gp18 strand	81	263

Movie S1 (separate file): The dynamic model of the phage T4 injection machinery reveals the dynamics of the contraction wave and the dynamics of the attached capsid/neck/tail tube assembly.

Supplemental References

[1] A. Maghsoodi, A. Chatterjee, I. Andricioaei, and N. C. Perkins, "Dynamic Model Exposes the Energetics and Dynamics of the Injection Machinery for Bacteriophage T4," *Biophys. J.*, vol. 113, no. 1, pp. 195–205, 2017.

[2] A. A. Aksyuk *et al.*, "The tail sheath structure of bacteriophage T4: A molecular machine for infecting bacteria," *EMBO J.*, vol. 28, no. 7, pp. 821–829, 2009.

[3] A. Eswar, N., Webb, B., Marti-Renom, M.A., Madhusudhan, M.S., Eramian, D., Shen, M.Y., Pieper, U. and Sali, "Comparative protein structure modeling using MODELLER," *Curr. Protoc. Bioinforma.*, vol. 15, no. 1, pp. 5–6, 2006.

[4] P. Ge, D. Scholl, P. G. Leiman, X. Yu, J. F. Miller, and Z. H. Zhou, "Atomic structures of a bactericidal contractile nanotube in its pre- and postcontraction states," vol. 22, no. 5, pp. 377–383, 2015.

[5] M. N. Nguyen and M. S. Madhusudhan, "Biological insights from topology independent comparison of protein 3D structures," vol. 39, no. 14, 2011.

[6] P. G. Leiman, P. R. Chipman, V. A. Kostyuchenko, V. V. Mesyanzhinov, and M. G. Rossmann, "Three-dimensional rearrangement of proteins in the tail of bacteriophage T4 on infection of its host," *Cell*, vol. 118, no. 4, pp. 419–429, 2004.

[7] E. F. Pettersen *et al.*, "UCSF Chimera - A visualization system for exploratory research and analysis," *J. Comput. Chem.*, vol. 25, no. 13, pp. 1605–1612, 2004.

[8] J. C. Phillips *et al.*, "Scalable molecular dynamics with NAMD," *J. Comput. Chem.*, vol. 26, no. 16, pp. 1781–1802, 2005.

[9] B. R. Brooks, R. E. Bruccoleri, B. D. Olafson, D. J. States, S. Swaminathan, and M. Karplus, "CHARMM: A program for macromolecular energy, minimization, and dynamics calculations," *J. Comput. Chem.*, vol. 4, no. 2, pp. 187–217, 1983.

[10] I. Andricioaei and M. Karplus, "On the calculation of entropy from covariance matrices of the atomic," *J. Chem. Phys.*, vol. 115, no. 14, pp. 6289–6292, 2001.

[11] Singiresu S. R, *Mechanical vibrations*, 4th ed. Prentice Hall, 2003.

[12] M. Taranova, A. D. Hirsh, N. C. Perkins, and I. Andricioaei, "Role of Microscopic Flexibility in Tightly Curved DNA," *J. Phys. Chem. B*, vol. 118, pp. 11028–11036, 2014.

[13] M. F. Moody, "Sheath of bacteriophage T4. III. Contraction mechanism deduced from partially contracted sheaths," *J. Mol. Biol.*, vol. 80, no. 4, pp. 613–635, 1973.

[14] J. Howard, *Mechanics of Motor Proteins and the Cytoskeleton*. Sinauer Associates, Sunderland, MA., 2001.

[15] A. Maghsoodi and N. Perkins, "Shear Deformation Dissipates Energy in Biofilaments," *Sci. Rep.*, vol. 8, no. 1, pp. 1–8, 2018.

[16] K. F. Graff, *Wave motion in elastic solids*. Courier Corporation, 2012.

[17] V. Vadillo-rodriguez and J. R. Dutcher, "Dynamic viscoelastic behavior of individual Gram-negative bacterial cells," *Soft Matter*, vol. 5, pp. 5012–5019, 2009.

[18] L. Redondo-morata, M. I. Giannotti, and F. Sanz, "AFM-Based Force-Clamp Monitors Lipid Bilayer Failure Kinetics," *Langmuir*, vol. 28, no. 15, pp. 6403–6410, 2012.

[19] J. T. Mika *et al.*, "Measuring the Viscosity of the Escherichia coli Plasma Membrane Using Molecular Rotors," *Biophysj*, vol. 111, no. 7, pp. 1528–1540, 2016.

[20] J. Kyte and R. F. Doolittle, "A simple method for displaying the hydropathic character of a protein," *J. Mol. Biol.*, vol. 157, no. 1, pp. 105–132, 1982.

[21] N. M. I. Taylor *et al.*, "Structure of the T4 baseplate and its function in triggering sheath contraction," *Nature*, vol. 533, no. 7603, pp. 346–352, 2016.

[22] M. P. Goertz, J. E. Houston, and X. Zhu, "Hydrophilicity and the Viscosity of Interfacial Water," no. 24, pp. 5491–5497, 2007.

[23] A. Fokine *et al.*, "The molecular architecture of the bacteriophage T4 neck," *J. Mol. Biol.*, vol. 425, no. 10, pp. 1731–1744, 2013.

[24] W. Jiang *et al.*, "Cryo-EM structure of the bacteriophage T4 isometric head at 3.3-Å resolution and its relevance to the assembly of icosahedral viruses," *Proc. Natl. Acad. Sci.*, vol. 114, no. 39, pp. E8184–E8193, 2017.